



Research paper

Versatile control of concentration gradients in non-fullerene acceptor-based bulk heterojunction films using solvent rinse treatments

Chang-Mok Oh ^{a,1}, Soyeong Jang ^{b,1}, Jihoon Lee ^b, Sung Heum Park ^{b,*}, In-Wook Hwang ^{a,*}

^a Advanced Photonics Research Institute, Gwangju Institute of Science and Technology, Gwangju, 61005, Republic of Korea

^b Department of Physics, Pukyong National University, Busan, 48513, Republic of Korea

Received 14 October 2020; revised 9 December 2020; accepted 8 January 2021

Available online 13 January 2021

Abstract

Solvent rinse treatments using polar methanol (MeOH) and nonpolar n-hexane have been developed for controlling material concentration gradients along the longitudinal direction of non-fullerene acceptor-based bulk heterojunction (BHJ) films comprised of electron donor polymer, PBDB-T and acceptor, ITIC-m. Before the used solvents (chlorobenzene with 1 vol% DIO) were completely evaporated, ITIC-m rich domains were formed at the top surface of the BHJ films after they were rinsed with MeOH, as evidenced by water contact angle, atomic force microscopy, time-of-flight secondary ion mass spectroscopy, which led to enhanced electron transport in the conventional structure of organic solar cells (OSCs). In contrast, after rinsing with n-hexane, ITIC-m rich domains were formed at the bottom surface of the films, which improved electron transport in the inverted structure OSCs. The enhanced carrier transports increased the PCEs (11.80% and 11.15%) in both conventional and inverted OSCs by 10.29% and 10.35% compared with control devices. The versatile control of material concentration gradients is determined to be feasible owing to the chemical interaction of the used substrates (glass, PEDOT:PSS, and ZnO) and rinsing solvents.

© 2021 Institute of Process Engineering, Chinese Academy of Sciences. Publishing services by Elsevier B.V. on behalf of KeAi Communications Co., Ltd. This is an open access article under the CC BY-NC-ND license (<http://creativecommons.org/licenses/by-nc-nd/4.0/>).

Keywords: Non-fullerene acceptor-based organic solar cells; Concentration gradients; Solvent rinse treatments

1. Introduction

Owing to their high flexibility, light-mass, and low fabrication cost via solution processing, organic solar cells (OSCs) are promising candidates for next-generation renewable energy source [1–3]. OSCs are generally fabricated using bulk heterojunction BHJ composites, comprised of bi-continuous networks of semiconducting polymer (electron) donors and small molecule acceptors. When photo-excited, BHJs initially generate excitons (electron–hole pairs), which are dissociated into charges at the interface of the donor and acceptor via an

ultrafast electron transfer process [4], and collected at the electrodes, leading to open-circuit voltage (V_{oc}) and short-circuit current (J_{sc}) in OSCs. To exhibit small carrier recombination loss for better power conversion efficiencies (PCEs) in OSCs, carrier generation and transport should be controlled in these processes. In recent OSCs, because of the increase in V_{oc} and J_{sc} , owing to decreased voltage loss [5,6] and extended absorption spectra, respectively, non-fullerene acceptors (NFAs) have exhibited better PCEs than conventional fullerene acceptors [7–16]. However, efforts are rarely made to optimise carrier generation and transportation in the NFA-based OSCs.

To achieve better PCEs in OSCs, the control of BHJ morphology is very important [11,17–19]. The morphology of BHJs should be controlled to demonstrate bi-continuous networks that are thinner than the length of exciton diffusion (i.e.,

* Corresponding authors.

E-mail addresses: spark@pknu.ac.kr (S.H. Park), hwangiw@gist.ac.kr (I.-W. Hwang).

¹ These authors contributed equally to this work.

less than 10 nm) [20,21]. The optimised BHJs should also exhibit high carrier (electron and hole) mobility and high charge separation [22–24]. In the fullerene-based OSCs case, BHJ morphology has been optimised by several treatments, including thermal [25,26] and solvent vapour [27] annealing, mixing solvent additives (e.g., 1,8-diodooctane (DIO)) with the polymer/fullerene-blend solution [28,29], solvent soaking [30–32], and post additive soaking [33,34]. All of these utilise self-assembly characteristics of organic materials, which are significantly influenced by processing environments.

Recently, alcohol-based solvent rinse treatments have been established to increase PCEs in fullerene-based OSCs. When polymer/fullerene composite films are rinsed with MeOH, acceptor (fullerene) rich domains are formed at the top surface of the film immediately after spinning the BHJ blend solution without drying the film. This improves the contact area, realises electron transport at the interface between BHJ and electron transport layers, and enhances PCEs in conventional OSC structures [30,31,35]. This treatment also removes residual (not evaporated) high boiling point solvents (chlorobenzene (CB) and DIO) [31], which is one of prerequisites for mass production of OSCs. The alcohol-based rinse treatments are relevant for fabricating efficient conventional structures of OSCs, because they create electron acceptor (fullerene) enriched domains at the top surface of the BHJ films, which are connected to electron transport layers. Inverted OSCs have better device efficiencies and lifetimes than conventional ones because of the absence of acidic and semi-transparent PEDOT:PSS as hole transporting layers and the inclusion of air-stable metals as top anodes [36,37]. However, alcohol rinse treatments of inverted OSCs are not beneficial because of the mismatch in the material concentration gradients, i.e., electron acceptor rich domains generated under hole transporting layers [35]. In inverted structures, acceptor deficient and thus donor (polymer) rich domains need to be formed at the top surface of the films.

In this study, we demonstrate that material concentration gradients in a non-fullerene-acceptor based BHJ composite, comprised of PBDB-T, poly[(2,6–4,8-bis(5-(2-ethylhexyl)thiophen-2-yl)-benzo[1,2-b:4,5-b']dithiophene)]-alt-(5,5-(10,3'-di-2-thienyl-5',7'-bis(2-ethylhexyl)benzo[10,2'-c:4',5'-c']dithiophene-4,8-dione)) and ITIC-m (3-(1,1-dicyanomethylene)-1-methyl-indanone)-5,5,11,11-tetrakis(4-hexylphenyl)-dithieno[2,3-d:2',3'-d']-s-indaceno[1,2-b:5,6-b']-dithiophene), which show high PCEs of over 10% and a high fill factor (FF) of approximately 78% [38,39], are flexibly controlled along the longitudinal direction of the films by solvent rinse treatments using polar MeOH and nonpolar n-hexane. From the data analyses, we determined that the ITIC-m molecules are flexibly redistributed by the solvent rinse before the used solvents are evaporated (chlorobenzene with 1 vol% DIO). The ITIC-m rich domains are created at the top and bottom surfaces of the films by rinsing with MeOH and n-hexane, respectively. The versatile redistribution of the ITIC-m is determined to be feasible by the chemical (nonpolar–nonpolar and polar–nonpolar) interactions of the used substrates (glass, ZnO, and PEDOT:PSS) and rinsing solvents (MeOH and n-hexane). From this study, we also

determined that exciton dissociation and electron mobility in the ITIC-m networks are improved by solvent rinse, owing to the self-assembly characteristics of organic materials, which is influenced by the surrounding (rinsing) solvents. The improvements in carrier transport and generation eventually leads to the enhancement of PCEs at over 11% in both conventional and inverted OSCs, compared with approximately 10% in the control devices. Our findings may provide new insights into BHJ control for better carrier transports in OSCs.

2. Results and discussion

Water contact angle (WCA) and atomic force microscope (AFM) phase images of PBDB-T, ITIC-m, and PBDB-T:ITIC-m films are presented in Fig. 1. Transmission electron microscopy (TEM) images of the films are given in Fig. S1. The data for BHJ films were measured before and after the solvent rinse. The pristine PBDB-T:ITIC-m film, hereafter denoted as reference, was fabricated following general procedures for processing additive methods, i.e., by spinning the PBDB-T:ITIC-m (1:1) blend solution containing 1 vol% DIO and drying at high vacuum conditions of less than 10^{-6} Torr for 1 h. The solvent-rinsed films were casted by spinning the blend solution and promptly rinsing with inert MeOH and n-hexane, i.e., immediately washing out the chlorobenzene and DIO.

Surface composition can be calculated by measuring the WCA of a blend film as each organic material exhibits an intrinsic WCA. The PBDB-T and ITIC-m exhibit intrinsic WCAs of 97.79° and 87.64° , respectively, indicative of the high surface energy of the ITIC-m (Fig. 1(a)). Moving from hexane-treated to reference and MeOH-treated ones, BHJ films exhibit a systematic decrease in WCA, i.e., from 94.43° to 92.81° and 91.31° (Fig. 1(a)). Using the Cassie–Baxter equation [40],

$$\cos\theta_{BHJ} = f \cos\theta_{PBDB-T} + (1 - f)\cos\theta_{ITIC-m},$$

where θ is the WCA of each component and f is the fraction of PBDB-T, we calculated the surface coverages of the ITIC-m, as indicated in Fig. 1(a) as 33.06%, 49.11%, and 63.90% in the hexane-treated, reference, and MeOH-treated films, respectively.

The increased ITIC-m coverage by the MeOH rinse is consistent with those determined for the fullerene-based BHJs. In previous reports, fullerene depletion layers were determined to be generated at the top surface of the films by slowly evaporating the residual DIO under a vacuum, apparently because of the surface energy, whereas the fullerene rich domains were formed at the top surface of the films by promptly washing out the DIO with MeOH, owing to the locking of the fullerenes during material redistribution [31]. The ITIC-m enriched film surface created by the MeOH rinse may be understood by following the previous description on the fullerene-based BHJs. However, the ITIC-m surface depleted by the n-hexane rinse has not been understood, especially when considering the similar low boiling points of MeOH and n-hexane at 64.7°C and 68.7°C , respectively.

To find the origin of material concentration gradients, we investigated the chemical interactions at the interface between

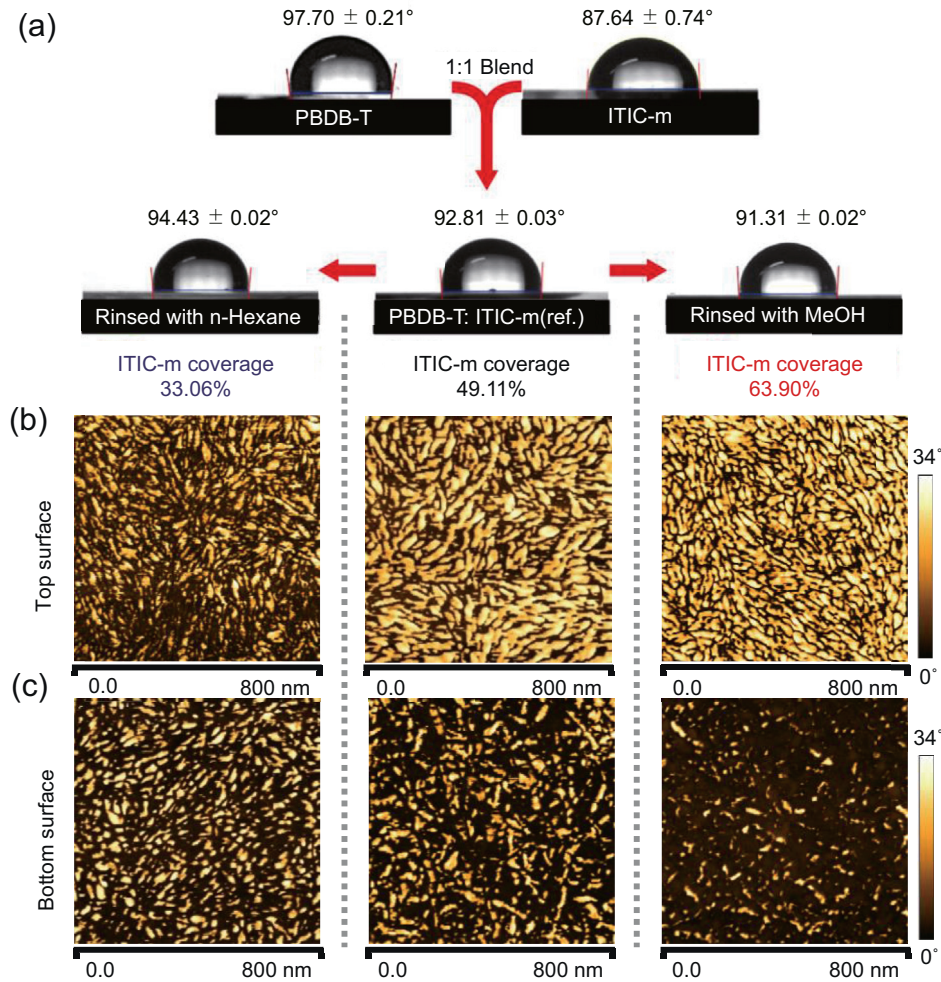


Fig. 1. (a) WCA images of PBDB-T, ITIC-m, and PBDB-T:ITIC-m BHI films. The WCA images measured before and after rinsing BHI films with n-hexane and MeOH are indicated in the left and right of the second row, respectively. The measured WCAs and calculated ITIC-m coverages are indicated. (b) AFM phase images obtained from top surface of n-hexane-treated, reference, and MeOH-treated BHI films. (c) AFM phase images obtained from bottom surface of the n-hexane-treated, reference, and MeOH-treated PBDB-T:ITIC-m films.

the used substrates (glass, PEDOT:PSS, and ZnO) and the rinsing solvents (MeOH and n-hexane), by measuring the contact angles of the solvents when dropped on their respective substrates (Fig. 2). In the measurement, a MeOH contact angle on the PEDOT:PSS layer was measured immediately, before the MeOH dissolved the PEDOT:PSS layer. When dropped, n-hexane and MeOH exhibit completely different behaviours in the solvent dispersion, i.e., much smaller contact angles were discovered for the n-hexane than those for the

MeOH. The MeOH exhibited contact angles of 11–14°, whereas the hexane exhibited contact angles of 5–8°. The smaller contact angles are indicative of better chemical interaction at the interface of nonpolar n-hexane and apparently nonpolar substrates (glass, PEDOT:PSS, and ZnO). In contrast, a poorer chemical interaction occurs at the interface between polar MeOH and the (nonpolar) substrates. In the hexane rinse, the ITIC-m may move to the bottom of the films because the DIO dissolves ITIC-m and is miscible with n-

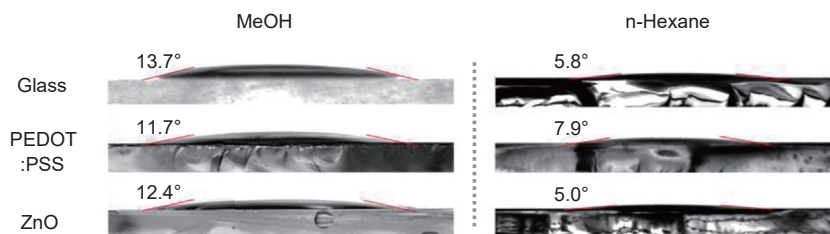


Fig. 2. MeOH (left) and n-hexane (right) contact angle images measured for glass, PEDOT:PSS, and ZnO substrates.

hexane, whereas in the MeOH rinse, the ITIC-m may move to the top surface of the films by following MeOH movements, despite the poor solubility of DIO in MeOH.

AFM phase images at the top and bottom surfaces of the films provide more insights into material concentration gradients (Fig. 1(b) and (c)). To obtain images at the bottom surface of the films, we spun coated BHI films on PEDOT:PSS-coated glasses and detached BHI films by dissolving PEDOT:PSS layers by putting the films into water. To isolate PBDB-T and ITIC-m, we measured the AFM images for a film, which was fabricated by spin coating the PBDB-T (dissolved in chlorobenzene) and dispersing a small amount of ITIC-m (dissolved in n-hexane containing 10 vol% DIO) on a glass. ITIC-m and PBDB-T exhibit bright and dark AFM phase images, respectively (Fig. S2).

As shown in Fig. 1(b) and (c), the coverage of ITIC-m is drastically changed at the top and bottom surfaces by rinsing with MeOH and n-hexane. By integrating the bright (ITIC-m) and dark (PBDB-T) areas of the top surface images, the ITIC-m coverages were calculated as 35.93%, 55.73%, and 65.22% in the hexane-treated, reference, and MeOH-treated films, which correlate with the corresponding WCA values (33.06%, 49.11%, and 63.90%). Note that in Fig. 1(c), the images obtained from the bottom of the films exhibit opposite behaviours, compared to those of the top surface. The ITIC-m rich and depleted domains are generated at the bottom by treating with n-hexane and MeOH, respectively. By integrating the bright and dark areas of the bottom surface images, the ITIC-m coverages were calculated as 33.91%, 27.74%, and 13.20% in the hexane-treated, reference, and MeOH-treated films. The reversed AFM phase images obtained for the top and bottom surfaces are indicative of the complete redistribution of the materials along the longitudinal direction of the films. In Fig. 1(b) and (c), we also determined that the domain sizes of the ITIC-m aggregates are decreased by immediately rinsing with MeOH and n-hexane at low boiling points of 64.7 °C and 68.7 °C, respectively. These results are indicative of the efficient overgrowth elimination of the ITIC-m aggregates, which generally occur when the high boiling point of solvents are slowly evaporated, i.e., chlorobenzene and DIO with boiling points equal to 132 °C and 365 °C, respectively. The smaller ITIC-m domains may be useful for better exciton dissociation in photo-excited BHJs.

A more complete picture of the material concentration gradients is provided via time-of-flight secondary ion mass spectroscopy (ToF-SIMS) (Fig. 3). The CN^- ion fragment, which solely exists in the ITIC-m, is plotted to monitor a change in relative ITIC-m concentration. BHI films consistently exhibit sharp CN^- peaks at the early sputtering time, $t < 30$ s, which is indicative of the segregation of the ITIC-m molecules at the top film surface, as demonstrated in the fullerene-based BHJs [34]. By moving from the hexane-treated to reference and MeOH-treated films, the systematic increase in the ITIC-m concentration observed at the early sputtering time, $t < 50$ s, i.e., at the film top surface (see the inset of Fig. 3), is found consistent with those determined from the WCA and AFM measurements. When compared with the

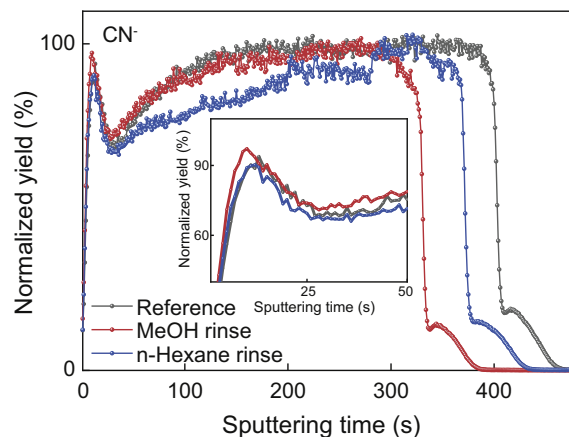


Fig. 3. In-depth distribution of CN^- ion in reference, MeOH-treated, and n-hexane-treated PBDB-T:ITIC-m BHI films, obtained using ToF-SIMS depth profiler.

reference, the hexane-treated film exhibits a more significant change in the ToF-SIMS spectral shape than the MeOH-treated one, which is indicative of a larger change in the material distribution induced by the n-hexane. We note that the residual solvents (chlorobenzene and 1 vol% DIO) are miscible with n-hexane but not with MeOH, despite the inert property of n-hexane and MeOH in dissolving PBDB-T and ITIC-m. In addition, ITIC-m dissolves well in DIO. Considering these, n-hexane may be deeply absorbed into the wet BHI films, leading to a complete redistribution of the ITIC-m along the longitudinal direction of the films.

The chemical structures of PBDB-T and ITIC-m, steady-state absorption, and photoluminescence (PL) spectra of BHI films are shown in Fig. 4. The PL spectra were divided by absorption intensity at an excitation wavelength of 400 nm to describe changes in the quantum yield of the PL. The shape of the absorption spectra of BHJs is an overlap of the absorption bands of PBDB-T and ITIC-m, which peaked at 624 and 697 nm, whereas the shape of the PL spectra is an overlap of the PL bands of PBDB-T and ITIC-m, peaking at 672 and 775 nm, respectively (Fig. 3). After the solvent (MeOH and n-hexane) rinses, the absorption intensity of PBDB-T and ITIC-m increases and decreases, respectively, whereas the PL intensity of PBDB-T and ITIC-m decreases. The reduced intensity of the ITIC-m absorption indicates that the solvent rinse partially removes the ITIC-m moiety, whereas the amplified intensity of the PBDB-T absorption demonstrates the restricted motion of polymer chains by enhanced intermolecular stacking, which may be induced by the removal of the ITIC-m. Compared to the pristine PBDB-T and ITIC-m films, the reference, MeOH-, and hexane-treated BHJs exhibit PBDB-T PL quenching by 98.5%, 99.2%, and 99.2%; and ITIC-m PL quenching by 95.4%, 97.0%, and 97.0%, respectively (Fig. S3). The enhanced PL quenching by the solvent rinse is indicative of improved exciton dissociation along the small material aggregates shown in Fig. 1.

To observe the effect of material concentration gradient control on device performance, we have fabricated conventional and inverted structure OSCs comprising ITO/

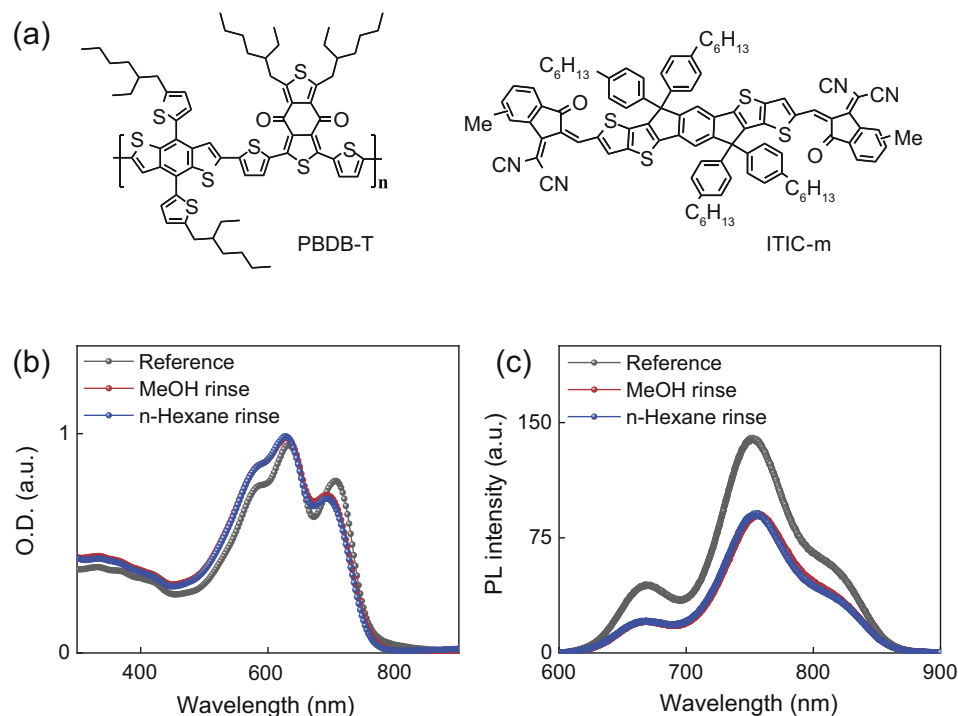


Fig. 4. (a) Chemical structures of PBDB-T and ITIC-m. (b) Absorption and (c) PL spectra of reference, MeOH-treated, and n-hexane-treated PBDB-T:ITIC-m BHJ films. An excitation wavelength of 400 nm was used in the PL measurements. The PL spectra were divided by absorption intensity at 400 nm to describe change in the quantum yield of the PL.

PEDOT:PSS/PBDB-T:ITIC-m/PDINO/Al and ITO/ZnO/PBDB-T:ITIC-M/MoO_x/Ag, in which the solvent rinse treatments were conducted on BHJ films before depositing electron and hole transport layers of PDINO and MoO_x; more details on the device fabrication were provided in the supporting information. An energy level diagram for each component used for fabricating OSCs is depicted in Fig. 5(a). Note that the energy levels are well organised for good electron and hole transports to the Al (cathode) and ITO (anode) in the conventional structure; and to the ITO (cathode) and Ag (anode) in the inverted structure, respectively. The current density–voltage (J–V) curves and characteristic device parameters (V_{oc} , J_{sc} , FF, and PCE) obtained from the OSCs are displayed in Fig. 5(b) and listed in Table 1.

Device performance is systematically influenced by the material concentration gradients that are controlled by the solvent rinse. In the conventional structure, where electron transfer occurs from the top surface of the BHJs to PDINO, PCE increases from 10.29% to 11.80% with the MeOH rinse, whereas it decreases to 9.93% with the hexane. In the inverted structure, where electron transfer occurs from the bottom surface of the BHJs to ZnO, the PCE increases from 10.35% to 11.15% with the n-hexane rinse, whereas it decreases to 9.31% with the MeOH. These results consistently demonstrate that material concentration gradients prepared by the solvent rinse successively operated for better and poorer carrier transports in the conventional and inverted structure of OSCs. Note that in Table 1, enhancements in the PCEs made by the solvent rinse predominantly result from improved J_{sc} rather than the FF and V_{oc} . In addition, the increased J_{sc} originate from

improved photocurrents in absorption of the PBDB-T and ITIC-m (Fig. 5(c) and Fig. S3). We also note that although the PL quenching of the PBDB-T and ITIC-m is consistently increased by the MeOH and n-hexane treatments (Fig. 4(c)), J_{sc} is increased and decreased by the n-hexane and MeOH treatment in the inverted structure cells (Fig. 5(b)). These results consistently indicate that feasible carrier recombination at the interface of the photoactive BHJ and carrier transporting layers play more crucial roles in determining the J_{sc} and PCE, rather than carrier generation after the photoexcitation of organics. The controlled material concentration gradients especially at the interface of BHJ and transporting layers may improve carrier transport and decrease carrier recombination losses.

To characterise the time for carrier transport within the OSCs, we measured time-resolved photoconductivity decays and fitted them using exponential functions (Fig. 6(a)). The decays for the conventional and inverted cells were fitted using single and double exponential functions (Fig. S4), and the weight averaged decay times are indicated at the right corner of each panel in Fig. 6(a). Faster carrier transport times (211 and 148 ns) than those of the reference (418 and 168 ns) were determined for the conventional and inverted OSCs processed with MeOH and n-hexane, respectively, which are consistent with the enhanced J_{sc} shown in Fig. 5 and Table 1. A slower carrier transport time (283 ns) than that of the reference (168 ns) was also determined in the MeOH-treated inverted cell, which is consistent with the decreased J_{sc} in Fig. 5. These results consistently demonstrate that by controlling the material concentration gradient, faster and therefore more efficient

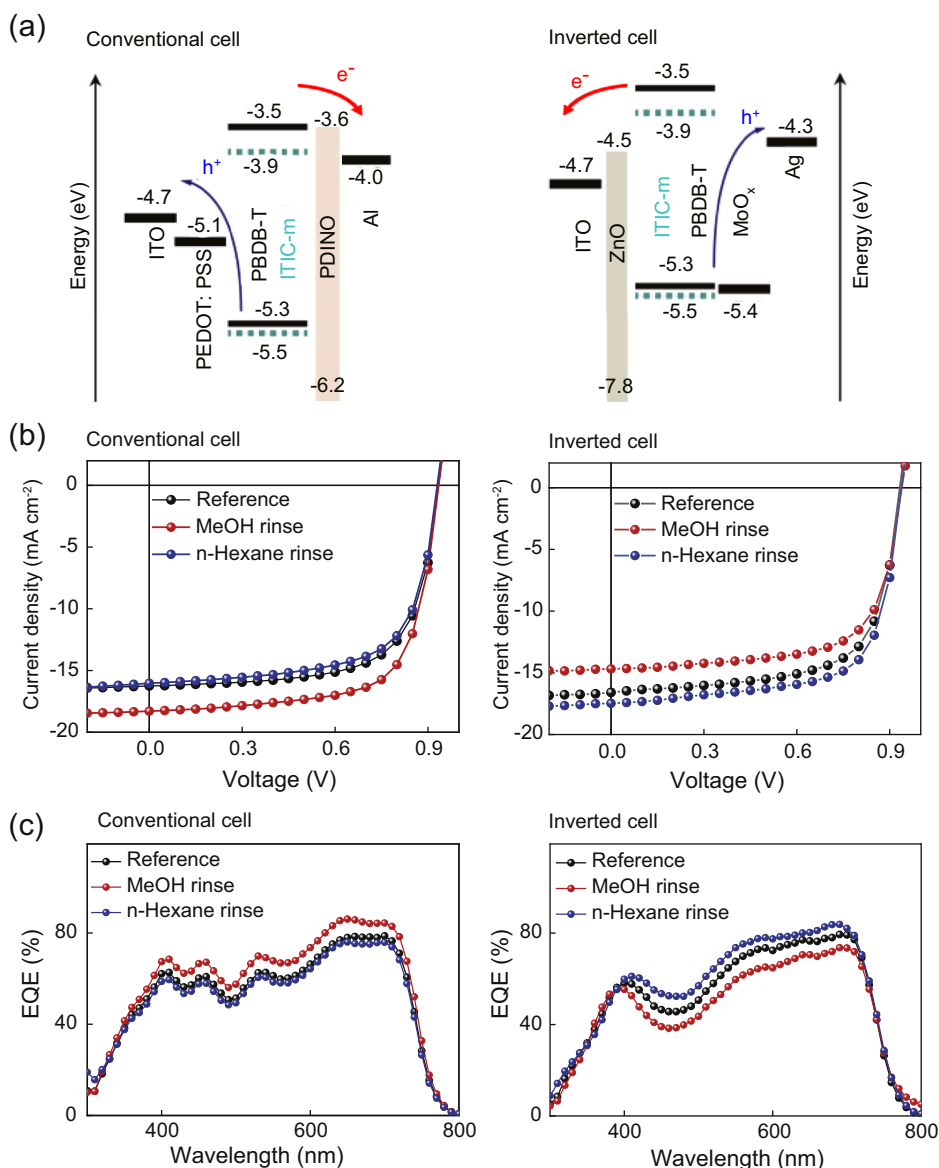


Fig. 5. (a) Schematic energy levels for individual components used to fabricate a conventional OSC comprising of ITO/PEDOT:PSS/PBDB-T:ITIC-m/PDINO/Al (left) and an inverted OSC comprising of ITO/ZnO/PBDB-T:ITIC-m/MoO_x/Ag (right). (b) J-V and (c) external quantum efficiency plots obtained from conventional (left) and inverted (right) structures of OSCs, fabricated using films of the reference, MeOH-treated, and n-hexane-treated PBDB-T:ITIC-m.

carrier transports are generated at the interface between BHJ and carrier transporting layers. In this interpretation, we have to note that the film thickness change may additionally contribute to the change in the TPC decay time. As shown in Fig. 3, the BHJ film thickness is decreased by ~10 nm and ~20 nm when rinsed with n-hexane and MeOH, respectively, compared to the 110 nm thickness of the reference pristine BHJ film. A shorter decay time (345 ns) than that of the reference (418 nm) may be observed for the conventional OSC processed with n-hexane, because of the decreased film thickness, despite of the controlled material concentration gradient. In contrast, a longer TPC decay time (283 ns) than that of the reference (168 ns), which is found for the MeOH-treated inverted cell, could not be explained by solely considering the decreased film thickness.

To further investigate carrier transports, we characterised the mobility of electrons and holes by measuring space charge limited currents (SCLCs), using a hole-only device ITO/PEDOT:PSS/active layer/MoO_x/Al and an electron-only device ITO/ZnO/active layer/PDINO/Al (Fig. 6(b) and S5). The reference, MeOH-, and hexane-treated devices show electron mobility of $1.72 \times 10^{-4} \text{ cm}^2 \text{ V}^{-1} \text{ s}^{-1}$, $3.88 \times 10^{-4} \text{ cm}^2 \text{ V}^{-1} \text{ s}^{-1}$, and $4.65 \times 10^{-4} \text{ cm}^2 \text{ V}^{-1} \text{ s}^{-1}$, respectively; and hole mobility of $6.65 \times 10^{-4} \text{ cm}^2 \text{ V}^{-1} \text{ s}^{-1}$, $6.21 \times 10^{-4} \text{ cm}^2 \text{ V}^{-1} \text{ s}^{-1}$, and $3.24 \times 10^{-4} \text{ cm}^2 \text{ V}^{-1} \text{ s}^{-1}$, respectively (Fig. 6(b)). The significant decrease in the hole mobility of the hexane-treated cell, compared to that of the methanol treated one, may result from the complete redistribution of the ITIC-m deduced by the well miscible property of the n-hexane and residual solvents (chlorobenzene and DIO). In contrast, as shown in

Table 1
Device characteristic parameters obtained from conventional and inverted structures of OSCs, fabricated using reference, MeOH-treated, and n-hexane-treated PBDB-T:ITIC-m films.

Conventional cell	J_{sc}^a (J_{sc}^b) (mA cm ⁻²)	V_{oc}^a (V_{oc}^b) (V)	FF ^a (FF) ^b (%)	PCE ^a (PCE) ^b (%)
Reference	16.25 (15.99 ± 0.19)	0.94 (0.94 ± 0.01)	0.67 (0.66 ± 0.03)	10.29 (9.89 ± 0.19)
MeOH rinse	18.29 (18.08 ± 0.20)	0.94 (0.94 ± 0.01)	0.68 (0.66 ± 0.03)	11.80 (11.4 ± 0.16)
n-Hexane rinse	16.03 (15.25 ± 0.25)	0.93 (0.93 ± 0.01)	0.66 (0.64 ± 0.03)	9.93 (9.61 ± 0.24)
Inverted cell	J_{sc}^a (J_{sc}^b) (mA cm ⁻²)	V_{oc}^a (V_{oc}^b) (V)	FF ^a (FF) ^b (%)	PCE ^a (PCE) ^b (%)
Reference	16.59 (15.58 ± 0.24)	0.94 (0.94 ± 0.01)	0.66 (0.64 ± 0.03)	10.35 (10.01 ± 0.25)
MeOH rinse	14.68 (14.48 ± 0.33)	0.94 (0.94 ± 0.01)	0.67 (0.65 ± 0.02)	9.31 (8.80 ± 0.27)
n-Hexane rinse	17.47 (17.24 ± 0.38)	0.94 (0.94 ± 0.01)	0.67 (0.65 ± 0.01)	11.15 (10.67 ± 0.33)

^a Photovoltaic performance obtained from the best device.

^b Photovoltaic performance averaged from over 16 devices with their deviation.

Fig. 1(b) and (c) the increased electron mobility of the MeOH and n-hexane-treated cells is interesting, especially when considering smaller aggregates for the BHJs. The increased electron mobility in thinner molecular networks may be beneficial for OSCs because of expected enhancements in both carrier generation and transport. We note that in Fig. 6(b), the solvent rinse-treated cells exhibit better charge balances ($\mu_h/\mu_e = 1.60$ and 1.44 for the MeOH and hexane-treated cells, respectively) than the reference ($\mu_h/\mu_e = 3.87$), despite

mobility changing by factors of 1–3. The balanced carrier transports may contribute to a decreased carrier recombination loss in the OSCs.

The increased carrier density by the solvent rinse is characterised by the measurement of steady-state photo-induced absorption spectra in the near-infrared regime (Fig. 6(c)). When photo-excitation occurred at 532 nm, i.e., photo-exciting both PBDB-T and ITIC-m, the solvent-rinsed BHJs exhibit larger PBDB-T polaron bands at 900–1200 nm [41],

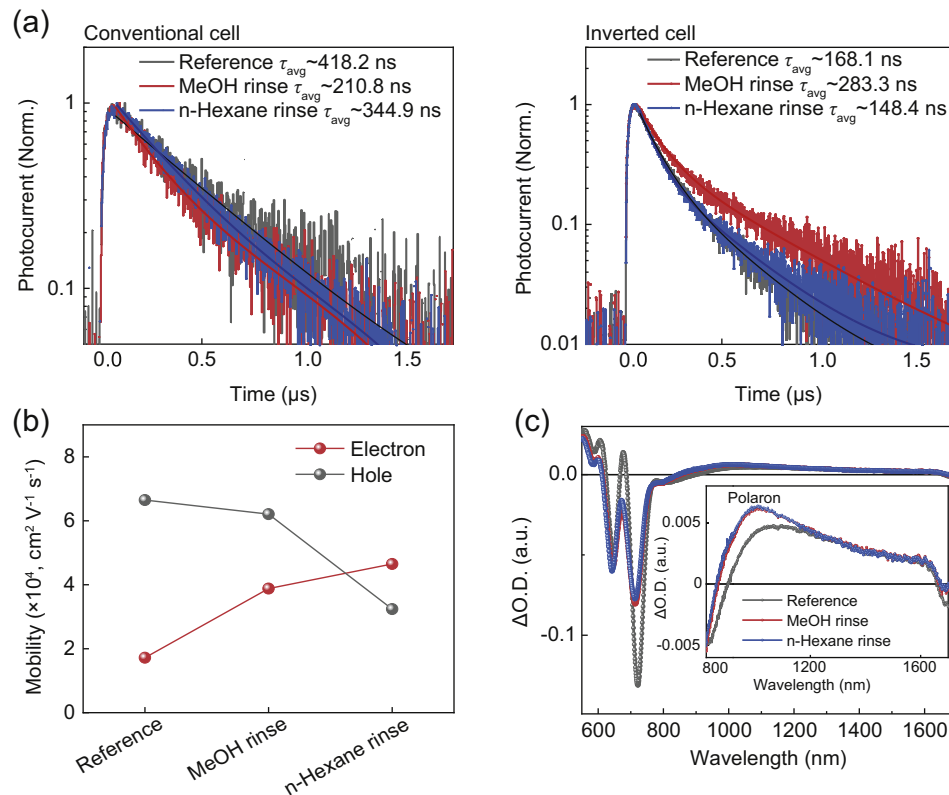


Fig. 6. (a) Time-resolved photoconductivity decays measured for conventional (left) and inverted (right) structures of OSCs, fabricated using films of reference, MeOH-treated, and n-hexane-treated PBDB-T:ITIC-m. (b) Hole and electron mobility characterised by SCLC measurements of hole and electron-only devices, fabricated using films of reference, MeOH-treated, and n-hexane-treated PBDB-T:ITIC-m. (c) Steady-state photo-induced absorption spectra of films of reference, MeOH-treated, and n-hexane-treated PBDB-T:ITIC-m. The excitation wavelength and intensity were 532 nm and approximately 100 mW, respectively.

than the reference. The amplified polaron bands may result from enhancements in carrier generation and transport, as evidenced by the measurement of PL and time-resolved photoconductivity, respectively.

3. Conclusions

Using polar MeOH and nonpolar n-hexane in the solvent rinse treatment, we have flexibly controlled the ITIC-m distribution along the longitudinal direction of PBDB-T:ITIC-m BHJ films and improved carrier transports in both conventional and inverted structures of OSCs, as demonstrated by the measurement of WCA, AFM, ToF-SIMS, SCLC, and time-resolved photoconductivity. The improved contact and carrier transport at the interface between BHJ and carrier transport layers i.e., PDINO and ZnO in the conventional and inverted OSCs, eventually increases the PCEs in both conventional and inverted structures of OSCs, i.e., from approximately 10% to over 11%. By measuring the solvent contact angles on the used substrates (glass, PEDOT:PSS, and ZnO), the source of material concentration gradients is determined to be a chemical interaction at the interface of the substrates and the rinsing solvents i.e., nonpolar–nonpolar and polar–nonpolar interactions. From the analyses of characteristic device parameters, we discovered that the enhancement in PCEs predominantly resulted from improved J_{sc} rather than FF and V_{oc} . Based on the analyses of the PL spectra, J-V curves, and incident photon-to-current efficiency (IPCE) spectra obtained for the accurate and inaccurate controlled BHJs in material concentration gradients, we determined that the improved J_{sc} originates from enhanced carrier transports, especially at the interface between BHJ and carrier transport layers, which may deactivate the carrier recombination loss.

Conflict of interest

The authors declare no conflict of interests.

Acknowledgements

This research study was supported by the Basic Science Research Program through the National Research Foundation of Korea (NRF) funded by the Ministry of Education, Science and Technology (NRF-2017R1D1A1B03030669), and the GIST Research Institute (GRI) APRI grant funded by GIST in 2020.

Appendix A. Supplementary data

Supplementary data to this article can be found online at <https://doi.org/10.1016/j.gee.2021.01.009>.

References

- [1] G. Yu, J. Gao, J.C. Hummelen, F. Wudl, A.J. Heeger, *Science* 270 (1995) 1789–1791.
- [2] Y. Cheng, S. Yang, C. Hsu, *Chem. Rev.* 109 (2009) 5868–5923.
- [3] G. Li, R. Zhu, Y. Yang, *Nat. Photon.* 6 (2012) 153–161.
- [4] I.-W. Hwang, D. Moses, A.J. Heeger, *J. Phys. Chem. C* 112 (2008) 4350–4354.
- [5] A. Tang, W. Song, B. Xiao, J. Guo, J. Min, Z. Ge, J. Zhang, Z. Wei, E. Zhou, *Chem. Mater.* 31 (2019) 3941–3947.
- [6] N. An, Y. Cai, H. Wu, A. Tang, K. Zhang, X. Hao, Z. Ma, Q. Guo, H.S. Ryu, H.Y. Woo, Y. Sun, E. Zhou, *Adv. Mater.* 32 (2020) 2002122.
- [7] S. Li, L. Ye, W. Zhao, H. Yan, B. Yang, D. Liu, W. Li, H. Ade, J. Hou, *J. Am. Chem. Soc.* 140 (2018) 7159–7167.
- [8] L. Meng, Y. Zhang, X. Wan, C. Li, X. Zhang, Y. Wang, X. Ke, Z. Xiao, L. Ding, R. Xia, H.L. Yip, Y. Cao, Y. Chen, *Science* 361 (2018) 1094–1098.
- [9] Z. Zheng, Q. Hu, S.Q. Zhang, D.Y. Zhang, J.Q. Wang, S.K. Xie, R. Wang, Y.P. Qin, W.N. Li, L. Hong, N.N. Liang, F. Liu, Y. Zhang, Z.X. Wei, Z.Y. Tang, T.P. Russell, J.H. Hou, H.Q. Zhou, *Adv. Mater.* 30 (2018) 1801801.
- [10] Y. Zhang, B. Kan, Y. Sun, Y. Wang, R. Xia, X. Ke, Y.Q. Yi, C. Li, H.L. Yip, X. Wan, Y. Cao, Y. Chen, *Adv. Mater.* 30 (2018) 1707508.
- [11] S. Li, W. Liu, C.Z. Li, M. Shi, H. Chen, *Small* 13 (2017) 1701120.
- [12] J. Hou, O. Inganäs, R.H. Friend, F. Gao, *Nat. Mater.* 17 (2018) 119–128.
- [13] C. Yan, S. Barlow, Z. Wang, H. Yan, A.K.Y. Jen, S.R. Marder, X. Zhan, *Nat. Rev. Mater.* 3 (2018) 18003.
- [14] G. Zhang, J. Zhao, P.C.Y. Chow, K. Jiang, J. Zhang, Z. Zhu, J. Zhang, F. Huang, H. Yan, *Chem. Rev.* 118 (2018) 3447–3507.
- [15] J. Zhang, H.S. Tan, X. Guo, A. Facchetti, H. Yan, *Nat. Energy* 3 (2018) 720–731.
- [16] P. Cheng, G. Li, X. Zhan, Y. Yang, *Nat. Photon.* 12 (2018) 131–142.
- [17] F. Zhao, C. Wang, X. Zhan, *Adv. Energy Mater.* 8 (2018) 1703147.
- [18] D. Deng, Y. Zhang, J. Zhang, Z. Wang, L. Zhu, J. Fang, B. Xia, Z. Wang, K. Lu, W. Ma, Z. Wei, *Nat. Commun.* 7 (2016) 13740.
- [19] J. Zhao, Y. Li, G. Yang, K. Jiang, H. Lin, H. Ade, W. Ma, H. Yan, *Nat. Energy* 1 (2016) 5027.
- [20] P.E. Shaw, A. Ruseckas, I.D.W. Samuel, *Adv. Mater.* 20 (2008) 3516–3520.
- [21] H. Wang, H.Y. Wang, B.R. Gao, L. Wang, Z.Y. Yang, X.B. Du, Q.D. Chen, J.F. Song, H.B. Sun, *Nanoscale* 3 (2011) 2280–2285.
- [22] S. Holliday, R.S. Ashraf, A. Wadsworth, D. Baran, S.A. Yousaf, C.B. Nielsen, C.-H. Tan, S.D. Dimitrov, Z. Shang, N. Gasparini, M. Alamoudi, F. Laquai, C.J. Brabec, A. Salgado, J.R. Durrant, I. McCulloch, *Nat. Commun.* 7 (2016) 11585.
- [23] N. Gasparini, A. Wadsworth, M. Moser, D. Baran, I. McCulloch, C.J. Brabec, *Adv. Energy Mater.* 8 (2018) 1703298.
- [24] Z. Du, W. Chen, Y. Chen, S. Qiao, X. Bao, S. Wen, M. Sun, L. Han, R. Yang, *J. Mater. Chem. A* 2 (2014) 15904–15911.
- [25] W. Ma, C. Yang, X. Gong, K. Lee, A.J. Heeger, *Adv. Funct. Mater.* 15 (2005) 1617–1622.
- [26] Z. Yi, W. Ni, Q. Zhang, M. Li, B. Kan, X. Wan, Y. Chen, *J. Mater. Chem. C* 2 (2014) 7247–7255.
- [27] G. De Luca, E. Treossi, A. Liscio, J.M. Mativetsky, L.M. Scolaro, V. Palermo, P. Samori, *J. Mater. Inside Chem.* 20 (2010) 2493–2498.
- [28] Y. Huang, X. Guo, F. Liu, L. Huo, Y. Chen, T.P. Russell, C.C. Han, Y. Li, J. Hou, *Adv. Mater.* 24 (2012) 3383–3389.
- [29] L. Ye, S. Zhang, W. Ma, B. Fan, X. Guo, Y. Huang, H. Ade, J. Hou, *Adv. Mater.* 24 (2012) 6335–6341.
- [30] L. Ye, Y. Jing, X. Guo, H. Sun, S. Zhang, M. Zhang, L. Huo, J. Hou, *J. Phys. Chem. C* 117 (2013) 14920–14928.
- [31] B.J. Tremolet de Villers, K.A. O'Hara, D.P. Ostrowski, P.H. Biddle, S.E. Shaheen, M.L. Chabinyc, D.C. Olson, N. Kopidakis, *Chem. Mater.* 28 (2016) 876–884.
- [32] T. Kong, H. Wang, W. Zhang, P. Fan, J. Yu, *J. Phys. D Appl. Phys.* 52 (2019) 195104.
- [33] I.W. Hwang, J. Kong, H.K. Yoo, K. Lee, *J. Phys. Chem. C* 119 (2015) 12896–12903.
- [34] J. Kong, I.W. Hwang, K. Lee, *Adv. Mater.* 26 (2014) 6275–6283.
- [35] S. Lu, K. Liu, D. Chi, S. Yue, Y. Li, Y. Kou, X. Lin, Z. Wang, S. Qu, Z. Wang, *J. Power Sources* 300 (2015) 238–244.
- [36] L. Chen, Z. Hong, G. Li, Y. Yang, *Adv. Mater.* 21 (2009) 1434–1449.

- [37] K. Wang, C. Liu, T. Meng, C. Yi, X. Gong, *Chem. Soc. Rev.* 45 (2016) 2937–2975.
- [38] S. Zhang, Y. Qin, J. Zhu, J. Hou, *Adv. Mater.* 30 (2018) 1800868.
- [39] H. Choi, J. Lee, C.M. Oh, S. Jang, H. Kim, M.S. Jeong, S.H. Park, I.W. Hwang, *J Mater. Chem. A* 7 (2019) 8805–8810.
- [40] D.M. Huang, S.A. Mauger, S. Friedrich, S.J. George, D. Dumitriu-LaGrange, S. Yoon, A.J. Moulé, *Adv. Funct. Mater.* 21 (2011) 1657–1665.
- [41] O.M. Awartani, B. Gautam, W. Zhao, R. Younts, J. Hou, K. Gundogdu, H. Ade, *J Mater. Chem. A* 6 (2018) 12484–12492.